

# The simulation of dynamic crack propagation using the cohesive segments method

Joris J.C. Remmers<sup>a,\*</sup>, René de Borst<sup>b</sup>, Alan Needleman<sup>c</sup>

<sup>a</sup>*Faculty of Aerospace Engineering, Delft University of Technology, P.O. Box 5058, 2600 GB Delft, The Netherlands*

<sup>b</sup>*Eindhoven University of Technology, Department of Mechanical Engineering, P.O. Box 513, 5600 MB Eindhoven, The Netherlands*

<sup>c</sup>*Division of Engineering, Brown University, Providence, RI 02912, USA*

Received 24 December 2006; received in revised form 24 June 2007; accepted 7 August 2007

## Abstract

The cohesive segments method is a finite element framework that allows for the simulation of the nucleation, growth and coalescence of multiple cracks in solids. In this framework, cracks are introduced as jumps in the displacement field by employing the partition of unity property of finite element shape functions. The magnitude of these jumps are governed by cohesive constitutive relations. In this paper, the cohesive segments method is extended for the simulation of fast crack propagation in brittle solids. The performance of the method is demonstrated in several examples involving crack growth in linear elastic solids under plane stress conditions: tensile loading of a block; shear loading of a block and crack growth along and near a bi-material interface.

© 2007 Elsevier Ltd. All rights reserved.

**Keywords:** Cohesive zone approach; Dynamic crack propagation; Partition of unity method; Cohesive segments method; Numerical stability

Fast crack propagation in brittle solids is often accompanied by diffuse cracking patterns such as crack branching and micro-crack nucleation away from the crack tip (Sharon et al., 1995). These phenomena play an important role in the overall cracking behaviour and in determining crack speeds, see for example (Ravi-Chandar and Knauss, 1984; Freund, 1998; Sharon and Fineberg, 1999). Whereas classical fracture mechanics analyses predict that tensile cracks in homogeneous isotropic solids can propagate at speeds as fast as the Rayleigh wave speed, crack speeds greater than half the Rayleigh wave speed are rarely observed in such solids.

The path that the crack follows and damage in front of the main crack may play important roles in limiting attainable crack speeds. Based on their experiments, Ravi-Chandar and Knauss (1984) argued that the occurrence of micro-cracks ahead of a main crack tip influences the overall speed of the main crack and plays a role in the crack branching process. Gao (1993) suggested a wavy-crack model that incorporates small deviations of the crack tip from its original crack path, hence reducing the apparent crack speed. Although

\*Corresponding author. Currently at Eindhoven University of Technology, Department of Mechanical Engineering, The Netherlands.  
E-mail address: [J.J.C.Remmers@tue.nl](mailto:J.J.C.Remmers@tue.nl) (J.J.C. Remmers).

these models are based on fairly idealised assumptions, they provide explanations for the described phenomena.

Various cohesive type finite element frameworks have been introduced in order to model crack nucleation, tortuous crack paths and micro-cracking in front of a main crack, e.g. (Needleman, 1987), (Camacho and Ortiz, 1996), (Xu and Needleman, 1994). Although these methods can address crack branching and micro-crack nucleation, some fundamental numerical problems remain. Since the cohesive surfaces are aligned with element boundaries, the orientation of cracks is restricted to a set of predefined paths. When the mesh is relatively dense, more or less arbitrary global crack paths can be captured, especially when advanced mesh structures are used (Papoulia et al., 2006). However, the initiation of branching can be affected by the limited number of possible paths and fine scale details of the crack path are lost. Another disadvantage arises in formulations as in (Xu and Needleman, 1994) where the cohesive surfaces have an initial non-zero compliance. The computed onset of crack branching is in good agreement with the preponderance of experimental observations. However, the presence of the cohesive surfaces reduces the overall stiffness of the body, especially in the vicinity of the crack tip, which reduces elastic wave speeds and can lead to spurious effects.

In Camacho and Ortiz (1996) cohesive surfaces are inserted at inter-element boundaries when a critical condition is met. This can be regarded as having cohesive surfaces that are rigid until the attainment of the critical condition. There is then no issue of a change in stiffness prior to crack nucleation. However, the abrupt introduction of cohesive surfaces can lead to numerical problems (Papoulia et al., 2003). Also, in (Falk et al., 2001), it was found that the predicted onset of crack branching was delayed or suppressed with initially rigid cohesive surfaces as compared with initially compliant cohesive surfaces. It remains to be determined whether this is an inherent consequence of having an initially rigid cohesive surface or is a consequence of the particular implementation in (Falk et al., 2001). This is an important distinction since Gao (1996) has shown that the limiting crack speed for a non-linear elastic solid can be much less than the Rayleigh wave speed associated with the zero stress elastic moduli. Thus, one possibility is that the good agreement with experiments seen in (Xu and Needleman, 1994) is due to the reduction in stiffness arising from the initially present cohesive surfaces.

The cohesive segments method as presented in (Remmers et al., 2003; Remmers, 2006) is an alternative finite element method where cohesive surfaces can be inserted within finite elements. As in Camacho and Ortiz (1996) cohesive segments are only inserted when needed. Since the crack direction is not tied to the mesh, cracks can nucleate with arbitrary orientations and can propagate in arbitrary directions.

In this paper, we present a time-dependent cohesive segments method, and use this to address dynamic fracture problems. In the next sections, the kinematic relations, the corresponding equilibrium equations and the implementation in a finite element formulation are discussed. After this, an extensive survey into the numerical stability of the time integration technique is presented. The application of the method is illustrated through several examples: (i) tensile loading of a block; (ii) shear loading of a block and (iii) crack growth along and near a bi-material interface.

## 1. Kinematic relations

The key feature of the cohesive segments approach is the possible emergence of *multiple* cohesive zones in a domain. Consider the domain  $\Omega$  with boundary  $\Gamma$  as shown in Fig. 1. The domain contains  $m$  discontinuities  $\Gamma_{d,j}$ , where  $j = 1 \dots m$ . Each discontinuity splits the domain into two parts, which are denoted accordingly as

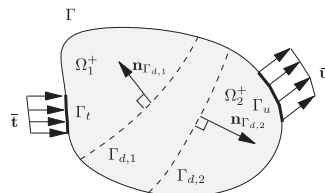


Fig. 1. Domain  $\Omega$  with two discontinuities,  $\Gamma_{d,1}$  and  $\Gamma_{d,2}$  (dashed lines). It is assumed that the discontinuities do not cross.

Table 1

An overview of different step functions that can be used to create a jump in the displacement field

Jump function	$\mathcal{H}_{\Gamma_{d,j}}^+$	$\mathcal{H}_{\Gamma_{d,j}}^-$	$h$
Heaviside	1	0	1
Symmetric	1/2	-1/2	1
Unit symmetric	1	-1	2

$\Omega_j^-$  and  $\Omega_j^+$ . For all discontinuities  $j$  in the domain, the following relation must hold:

$$\Omega_j^- \cup \Omega_j^+ = \Omega \quad \forall j = 1 \dots m. \quad (1)$$

The displacement field in the domain  $\Omega$  consists of a continuous displacement field  $\hat{\mathbf{u}}$  plus  $m$  additional continuous displacement fields  $\tilde{\mathbf{u}}_j$  (Belytschko and Black, 1999; Wells and Sluys, 2001; Daux et al., 2000):

$$\mathbf{u}(\mathbf{x}, t) = \hat{\mathbf{u}}(\mathbf{x}, t) + \sum_{j=1}^m \mathcal{H}_{\Gamma_{d,j}}(\mathbf{x}) \tilde{\mathbf{u}}_j(\mathbf{x}, t), \quad (2)$$

where  $\mathbf{x}$  denotes the position of a material point,  $t$  is time and  $\mathcal{H}_{\Gamma_{d,j}}$  is a step function, associated to the discontinuity  $\Gamma_{d,j}$ :

$$\mathcal{H}_{\Gamma_{d,j}} = \begin{cases} \mathcal{H}^+ & \text{if } \mathbf{x} \in \Omega_j^+, \\ \mathcal{H}^- & \text{if } \mathbf{x} \in \Omega_j^-. \end{cases} \quad (3)$$

The magnitude of the step  $h$  in this function is defined as

$$h = \mathcal{H}^+ - \mathcal{H}^-. \quad (4)$$

A number of possible step functions are listed in Table 1. Assuming a small strain formulation, the strain field is found by taking the derivative of the displacement field (2) with respect to the position of a material point in the body  $\mathbf{x}$ :

$$\varepsilon(\mathbf{x}, t) = \nabla^s \hat{\mathbf{u}}(\mathbf{x}, t) + \sum_{j=1}^m \mathcal{H}_{\Gamma_{d,j}}(\mathbf{x}) \nabla^s \tilde{\mathbf{u}}_j(\mathbf{x}, t), \quad \mathbf{x} \notin \Gamma_{d,j}, \quad (5)$$

where a superscript  $s$  denotes the symmetric part of the differential operator. Note that because of the discontinuous nature of the displacement field, the strain field can be discontinuous as well. At the internal boundaries  $\Gamma_{d,j}$ , the strains are not defined. There, the magnitude of the displacement jump

$$\mathbf{v}_j(\mathbf{x}, t) = h \tilde{\mathbf{u}}_j(\mathbf{x}, t), \quad (6)$$

is the relevant kinematic quantity with  $h$  defined in Table 1.

## 2. Equilibrium equations

The linear momentum balance equations for the domain  $\Omega$  including inertia terms, but without body forces, are equal to

$$\rho \ddot{\mathbf{u}} - \nabla \cdot \boldsymbol{\sigma} = \mathbf{0}, \quad \mathbf{x} \in \Omega, \quad (7)$$

where  $\rho$  is the density of the material and  $\boldsymbol{\sigma}$  is the Cauchy stress in the bulk material. It is assumed that the stress rate  $\dot{\boldsymbol{\sigma}}$  of the bulk material is a function of the strain rate  $\dot{\boldsymbol{\varepsilon}}$  as defined in Eq. (5):

$$\dot{\boldsymbol{\sigma}} = \mathbf{C} \dot{\boldsymbol{\varepsilon}}, \quad (8)$$

where  $\mathbf{C}$  is the tangent stiffness of the bulk material. In principle, any constitutive formulation can be used, but in the context of this paper, a rate independent, linear elastic behaviour is assumed.

The acceleration of a material point denoted by  $\ddot{\mathbf{u}}$  can be found by differentiating the displacement field, Eq. (2) twice with respect to time:

$$\ddot{\mathbf{u}}(\mathbf{x}, t) = \ddot{\mathbf{u}}(\mathbf{x}, t) + \sum_{j=1}^m \mathcal{H}_{\Gamma_{d,j}}(\mathbf{x}) \ddot{\mathbf{u}}_j(\mathbf{x}, t), \quad (9)$$

where  $(\cdot)$  denotes the second time derivative:  $\partial^2(\cdot)/\partial t^2$ . The corresponding boundary conditions for the external boundary and the discontinuities are, respectively:

$$\begin{aligned} \mathbf{n}_t \cdot \boldsymbol{\sigma} &= \bar{\mathbf{t}}, & \mathbf{x} \in \Gamma_t, \\ \mathbf{u} &= \bar{\mathbf{u}}, & \mathbf{x} \in \Gamma_u, \\ \mathbf{n}_{d,j} \cdot \boldsymbol{\sigma} &= \mathbf{t}_j, & \mathbf{x} \in \Gamma_{d,j}, \end{aligned} \quad (10)$$

where  $\bar{\mathbf{t}}$  are the prescribed tractions on  $\Gamma_t$  with outward normal vector  $\mathbf{n}_t$  and  $\bar{\mathbf{u}}$  is the prescribed displacement on external boundary  $\Gamma_u$ ;  $\mathbf{t}_j$  are the tractions at discontinuity  $\Gamma_{d,j}$ , which are defined by the cohesive constitutive relation, which relates tractions rates  $\dot{\mathbf{t}}_j$  to the velocity of the displacement jump  $\dot{\mathbf{v}}_j$ :

$$\dot{\mathbf{t}}_j = \mathbf{T} \dot{\mathbf{v}}_j. \quad (11)$$

Here,  $\mathbf{T}$  is the tangent stiffness of the traction separation law. The cohesive constitutive relation will be discussed in more detail in Section 3.

Equilibrium can be expressed in a weak form by multiplication with an admissible variational displacement field  $\delta \mathbf{u}$ :

$$\int_{\Omega} \delta \mathbf{u} \cdot (\rho \ddot{\mathbf{u}}) d\Omega + \int_{\Omega} \delta \mathbf{u} \cdot (\nabla \cdot \boldsymbol{\sigma}) d\Omega = 0. \quad (12)$$

In line with previous derivations, it is assumed that the space of the admissible variation  $\delta \mathbf{u}$  is the same as the field of the actual displacements, Eq. (2):

$$\delta \mathbf{u} = \delta \hat{\mathbf{u}} + \sum_{j=1}^m \mathcal{H}_{\Gamma_{d,j}} \delta \tilde{\mathbf{u}}_j. \quad (13)$$

Similarly, the admissible displacement jump  $\delta \mathbf{v}_j$  at the internal boundary  $\Gamma_{d,j}$  can be written as, see Eq. (6):

$$\delta \mathbf{v}_j = h \delta \tilde{\mathbf{u}}_j. \quad (14)$$

Inserting the strain and the acceleration field (9), applying Gauss' theorem, eliminating some of the Heaviside functions by changing the integration domain and incorporating the boundary conditions, the momentum balance (12), can be written as

$$\begin{aligned} & \int_{\Omega} \rho \delta \hat{\mathbf{u}} \cdot \ddot{\mathbf{u}} d\Omega + \sum_{j=1}^m \int_{\Omega} \mathcal{H}_{\Gamma_{d,j}} \rho \left( \delta \tilde{\mathbf{u}}_j \cdot \ddot{\mathbf{u}} + \delta \hat{\mathbf{u}} \cdot \ddot{\mathbf{u}}_j \right) d\Omega \\ & + \sum_{j=1}^m \sum_{k=1}^m \int_{\Omega} \mathcal{H}_{\Gamma_{d,j}} \mathcal{H}_{\Gamma_{d,k}} \rho \delta \tilde{\mathbf{u}}_j \cdot \ddot{\mathbf{u}}_k d\Omega + \int_{\Omega} \nabla^s \delta \hat{\mathbf{u}} : \boldsymbol{\sigma} d\Omega \\ & + \sum_{j=1}^m \int_{\Omega} \mathcal{H}_{\Gamma_{d,j}} \nabla^s \delta \tilde{\mathbf{u}}_j : \boldsymbol{\sigma} d\Omega + \sum_{j=1}^m \int_{\Gamma_{d,j}} h \delta \tilde{\mathbf{u}}_j \cdot \mathbf{t}_j d\Gamma \\ & = \int_{\Gamma_t} \delta \hat{\mathbf{u}} \cdot \bar{\mathbf{t}} d\Gamma + \sum_{j=1}^m \int_{\Gamma_t} \mathcal{H}_{\Gamma_{d,j}} \delta \tilde{\mathbf{u}}_j \cdot \bar{\mathbf{t}} d\Gamma. \end{aligned} \quad (15)$$

The first three terms in the equation represent the inertia of the body, whereas the remaining terms are related to the internal forces, the cohesive tractions and the applied external tractions, respectively.

### 3. Implementation aspects

The spatial discretisation of the system of equations relies on the partition of unity property of finite element shape functions as described by Babuška and Melenk (1997). The displacement field in Eq. (2) can be written in the following discrete form (Belytschko and Black, 1999; Wells and Sluys, 2001):

$$\mathbf{u} = \mathbf{N}\mathbf{a} + \sum_{j=1}^m \mathcal{H}_{\Gamma_{d,j}} \mathbf{N}\mathbf{b}_j. \quad (16)$$

Here, the vector  $\mathbf{a}$  contains the regular nodal degrees of freedom of the element and  $\mathbf{b}_j$  contains the additional nodal degrees of freedom associated with discontinuity  $\Gamma_{d,j}$ . Note that the magnitude of each displacement jump is supported by a unique set of degrees of freedom  $\mathbf{b}_j$ . As a result, multiple discontinuities in the same element can be simulated, which is necessary for the correct implementation of branching or coalescing cracks. The matrix  $\mathbf{N}$  contains the conventional element shape functions. The discretised acceleration can be found by differentiating the discrete displacement field, Eq. (16) twice with respect to time:

$$\ddot{\mathbf{u}} = \mathbf{N}\ddot{\mathbf{a}} + \sum_{j=1}^m \mathcal{H}_{\Gamma_{d,j}} \mathbf{N}\ddot{\mathbf{b}}_j. \quad (17)$$

The discrete displacement jump at the discontinuity  $\Gamma_{d,j}$  is equal to, see also Eq. (6):

$$\mathbf{v}_j = \mathbf{H}\mathbf{b}_j = h\mathbf{N}\mathbf{b}_j. \quad (18)$$

Inserting these expressions and the discrete admissible variation into Eq. (15) and taking the variations  $\delta\mathbf{a}$  and  $\delta\mathbf{b}_j$ , respectively, gives the following set of momentum balance equations:

$$\begin{bmatrix} \mathbf{M}_{aa} & \mathbf{M}_{ab_1} & \dots & \mathbf{M}_{ab_m} \\ \mathbf{M}_{ab_1} & \mathbf{M}_{b_1b_1} & \dots & \mathbf{M}_{b_1b_m} \\ \vdots & \vdots & \ddots & \vdots \\ \mathbf{M}_{ab_m} & \mathbf{M}_{b_1b_m} & \dots & \mathbf{M}_{b_mb_m} \end{bmatrix} \begin{bmatrix} \ddot{\mathbf{a}} \\ \ddot{\mathbf{b}}_1 \\ \vdots \\ \ddot{\mathbf{b}}_m \end{bmatrix} = \begin{bmatrix} \mathbf{f}_a^{\text{ext}} \\ \mathbf{f}_{b_1}^{\text{ext}} \\ \vdots \\ \mathbf{f}_{b_m}^{\text{ext}} \end{bmatrix} - \begin{bmatrix} \mathbf{f}_a^{\text{int}} \\ \mathbf{f}_{b_1}^{\text{int}} \\ \vdots \\ \mathbf{f}_{b_m}^{\text{int}} \end{bmatrix}. \quad (19)$$

The terms in the mass matrix  $\mathbf{M}$  are

$$\mathbf{M}_{aa} = \int_{\Omega} \rho \mathbf{N}^T \mathbf{N} d\Omega, \quad (20)$$

$$\mathbf{M}_{ab_j} = \int_{\Omega} \mathcal{H}_{\Gamma_{d,j}} \rho \mathbf{N}^T \mathbf{N} d\Omega, \quad (21)$$

$$\mathbf{M}_{b_jb_k} = \int_{\Omega} \mathcal{H}_{\Gamma_{d,j}} \mathcal{H}_{\Gamma_{d,k}} \rho \mathbf{N}^T \mathbf{N} d\Omega. \quad (22)$$

Note that this element mass matrix is completely filled. The components of the internal force vector,  $\mathbf{f}^{\text{int}}$ , are given by

$$\mathbf{f}_a^{\text{int}} = \int_{\Omega} \mathbf{B}^T \boldsymbol{\sigma} d\Omega, \quad (23)$$

$$\mathbf{f}_{b_j}^{\text{int}} = \int_{\Omega} \mathcal{H}_{\Gamma_{d,j}} \mathbf{B}^T \boldsymbol{\sigma} d\Omega + \int_{\Gamma_{d,j}} \mathbf{H}^T \mathbf{t}_j d\Gamma, \quad (24)$$

whereas the external force vector  $\mathbf{f}^{\text{ext}}$  is given by

$$\mathbf{f}_a^{\text{ext}} = \int_{\Gamma_t} \mathbf{N}^T \bar{\mathbf{t}} d\Gamma, \quad (25)$$

$$\mathbf{f}_{b_j}^{\text{ext}} = \int_{\Gamma_t} \mathcal{H}_{\Gamma_{d,j}} \mathbf{N}^T \bar{\mathbf{t}} d\Gamma. \quad (26)$$

The governing equations have been derived in a general way and can be implemented in any kind of continuum element as long as the underlying shape functions obey the partition-of-unity property. Herein, attention is confined to the implementation in two-dimensional continuum elements with a linear elastic plane strain or plane stress constitutive relation for the bulk material, (Remmers, 2006).

The life of a micro-crack can be divided into three stages: the nucleation, the growth and finally the coalescence with other micro-cracks. In all cases, the same criterion is used to determine when and in which direction a segment is created or extended. In order to arrive at a consistent numerical formulation, this fracture criterion is related to the cohesive constitutive relation that governs the debonding process of a cohesive segment.

When the stress state in a specific integration point in the bulk material is such that a critical cohesive traction is reached, a new cohesive segment is added. The segment, which is assumed to be straight, crosses this integration point and is extended into the neighbouring elements until it touches the outer boundaries of these elements, see Fig. 2. The patch of neighbouring elements consists of all elements that share one of the nodes of the central element that contains the integration point in which the criterion was violated. The nodes that support these outer boundaries are not enhanced in order to guarantee a zero crack opening at the tips of the new segments.

A new segment does not immediately reduce the high stresses in the bulk material. Depending on the fracture toughness of the material and the magnitude of the load step, the stresses in the vicinity of the centre of the new segment will only slowly fade away. Even so, especially in dynamic simulations, it can occur that the stress state locally increases for a small period of time. To prevent new segments from being nucleated in the same position in a short period of time, an element and its neighbours can be the source of a new segment only once in a simulation.

The extension of a cohesive segment is carried out as in (Wells and Sluys, 2001). When the stress state at the tip attains the critical cohesive traction at a specified angle, the segment is extended into the next element in that direction, until it touches the boundary of that element. Since the stress state at the tip is not known exactly, the stresses are estimated by calculating the average stress state in the vicinity using a Gauss averaging criterion. The most accurate prediction of the direction of the crack was obtained when the averaging length  $l_a$  was chosen to be three times the specific element length in the mesh around the tip. As a result, the stress state is underestimated and in general, the cohesive segment is extended somewhat too late. In the original formulation by Wells and Sluys (2001), this did not appear to be a serious problem, but in the cohesive segments method, a discrepancy is created since the fracture criterion is used to determine both the nucleation of a segment as well as its extension (Remmers, 2006). Nucleation is based on the stress state in a single integration point instead of an average stress state that is normally too low. Hence, the nucleation of a new segment is favoured over the extension of an existing segment, which will hamper quantitative analysis of diffuse fracture problems. In transient simulations this problem is even more pronounced.

For this reason two alternative approaches have been examined. In the first approach, different stress states are used to determine (i) *when* a segment should be extended and (ii) *in which direction* the segment should be extended. In practise, the method works as follows. At the tip of a segment, the stress state in the nearest integration point, which is in general a good representative of the peak stress, is monitored. When this stress

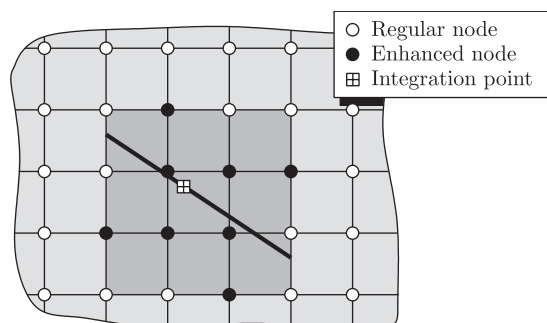


Fig. 2. Creation of a new cohesive segment (bold line) in virgin material. The segment crosses the integration point in the bulk material in which the criterion was violated. The segment is stretched until it touches the boundary of the patch of elements (grey area) that share the nodes of the element in which the peak cohesive traction was reached.

state violates the criterion for extension, a second, averaged stress state is determined, based on a number of integration points within a certain radius of the tip. The direction of the extension is then based on this averaged stress state. Note that the averaged stress state can be significantly smaller than the peak stress.

The advantages of this approach are that the segment is extended at the correct load step and that it is extended in the right direction. However, this method is unreliable in situations where mode transitions become an important factor. An example of mode transition is observed in dynamic shear failure experiments (Kalthoff and Winkler, 1988). Here, the direction of crack propagation depends on the magnitude of the applied load. For low impact velocities, the crack propagates at an angle of  $70^\circ$  with respect to the initial crack, whereas at high impact velocities, the crack propagates nearly straight. The proposed method is able to capture a transition in the direction of crack growth, but the adiabatic shear band seen experimentally cannot be modelled because of the restriction to linear elastic material response. Furthermore, the impact velocity for which the crack growth direction changes cannot be captured accurately, since the criterion is based on inconsistent stress states.

In an alternative approach, both the creation as well as the extension of a cohesive segment are based on averaged stress states. A single average length  $l_a$  is used for all cases. In order to reduce the computational effort, a new segment can only nucleate at one point for each element, e.g. the geometric centre of the element. In both situations, the average stress state is used to determine both the instance as well as the direction of creation or extension. Obviously, the critical condition for adding a cohesive segment will occur with some delay, but the creation of a new segment is no longer favoured over the extension of an existing one.

A key feature of the method is the possibility to have multiple, interacting cohesive segments. To accommodate this, each cohesive segment is supported by a unique set of additional degrees of freedom. When two segments meet within a single element, the nodes that support the elements are enhanced twice. Consider the situation depicted in Fig. 3(a), in which segment II is approaching another segment (I). When the fracture criterion at the tip of segment II is violated, the segment is extended accordingly. The position of segment I marks a discontinuity and can therefore be considered as a free edge in the material. Hence, segment two is only extended until it touches segment I, see Fig. 3(b). Since this segment forms a free edge, there is no new tip for segment II and all nodes of the corresponding element are enhanced.

Crack branching is taken care of automatically. When the fracture criterion in an integration point in the vicinity of an existing segment is violated, a new segment is created which may cross the existing one, see Fig. 4. In that case, the new segment only contains a single tip.

In order to arrive at an unbiased stress-based formulation, the criterion for adding a cohesive segment is based on an effective traction (Camacho and Ortiz, 1996). From a stress  $\sigma$  normal and shear tractions  $t_n$  and  $t_s$  can be computed along an axis  $\eta$ , which is rotated by an angle  $\theta$  with respect to the  $x$ -axis, see Fig. 5:

$$t_n = \mathbf{n}^T \boldsymbol{\sigma} \mathbf{n}, \quad t_s = \mathbf{s}^T \boldsymbol{\sigma} \mathbf{n}, \quad (27)$$

where  $\mathbf{n}$  and  $\mathbf{s}$  are the unit normal and tangent vectors to the  $\eta$ -axis, respectively:

$$\mathbf{n} = [-\sin \theta, \cos \theta]^T, \quad \mathbf{s} = [\cos \theta, \sin \theta]^T. \quad (28)$$

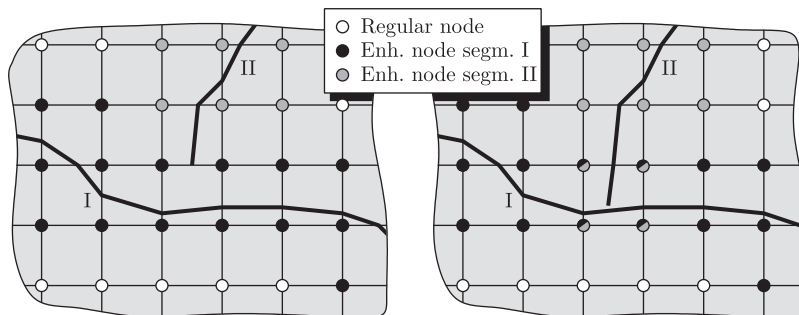


Fig. 3. Merging of two cohesive segments (bold lines). Segment II is extended until it touches segment I (right picture). Segment I can be regarded as a free edge so that segment II will not have a tip in this case. Consequently, all nodes of the element will be enhanced in order to support displacement discontinuity of segment II. Note that the nodes of these elements are enhanced twice.

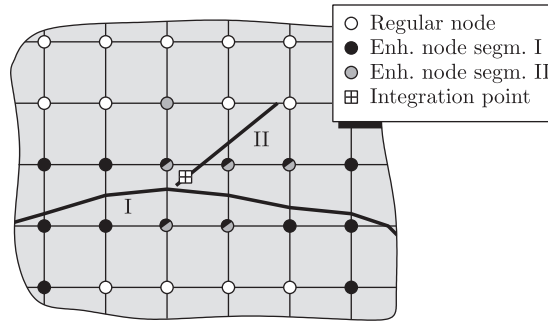


Fig. 4. Crack branching. When the effective traction in an integration point near an existing segment (I) exceeds the cohesive strength, a new segment (II) is created. This new segment is extended until it touches either the boundary of its neighbour elements or the existing segment (I). In the situation depicted in the figure, the new segment only has one tip.

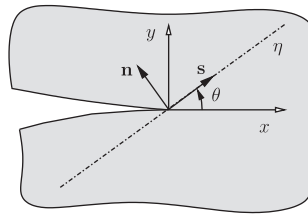


Fig. 5. Calculation of the effective traction  $t_{\text{eff}}$  along an imaginary axis  $\eta$  at an angle  $\theta$  with respect to the  $x$ -axis.

The normal and shear tractions  $t_n$  and  $t_s$  can be used to construct an effective traction  $t_{\text{eff}}$  which is a function of the angle  $\theta$  of the  $\eta$ -axis:

$$t_{\text{eff}}(\theta) = \sqrt{\langle t_n \rangle^2 + \frac{1}{\beta} t_s^2}, \quad (29)$$

where  $\langle \cdot \rangle$  are the McCauley brackets, and  $\beta$  is a scaling factor that is typically set to 2.3 (Camacho and Ortiz, 1996). For a given stress  $\sigma$ , the effective traction  $t_{\text{eff}}$  can be determined for all orientations  $\theta$  of the axis  $\eta$ . The angle for which the effective traction exceeds the maximum allowable traction  $t_{\text{max}}$  first is the direction in which the crack will propagate. This angle  $\theta_{\text{max}}$  can be found by solving a minimisation problem. It can be demonstrated that for mode-I crack propagation, this direction is identical to the direction perpendicular to the principal stress angle (Wells and Sluys, 2001). However, in this formulation, a distinction is made between a tensile and a compressive stress. Moreover, the contribution of the shear stress can be scaled using the  $\beta$  parameter.

To avoid sudden jumps in stresses when a discontinuity is inserted, the constitutive behaviour of the cohesive segment is related to the stress state in the bulk material that violates the fracture criterion. The initial tractions in this irreversible cohesive relation are taken to be equal to the normal and shear tractions in the bulk material at the exact moment of nucleation, see Eq. (27), see also (Camacho and Ortiz, 1996).

For the debonding behaviour, a distinction is made between normal and shear behaviour. When the normal traction component  $t_{n,0}$  is positive, the cohesive segment is assumed to open as a tensile crack. The cohesive tractions in both normal and shear directions  $t_n$  and  $t_s$  decrease monotonically from their initial values  $t_{n,0}$  and  $t_{s,0}$  to zero as a function of the normal displacement jump, see Fig. 6(a):

$$t_n = t_{n,0} \left( 1 - \frac{v_n}{v_{n,\text{cr}}} \right), \quad t_s = t_{s,0} \left( 1 - \frac{v_n}{v_{n,\text{cr}}} \right) \text{sgn}(v_s), \quad (30)$$

where  $v_n$  and  $v_s$  are the normal and sliding displacement, respectively,  $\text{sgn}(\square)$  is the signum function:

$$\text{sgn}(x) = \frac{x}{|x|}. \quad (31)$$



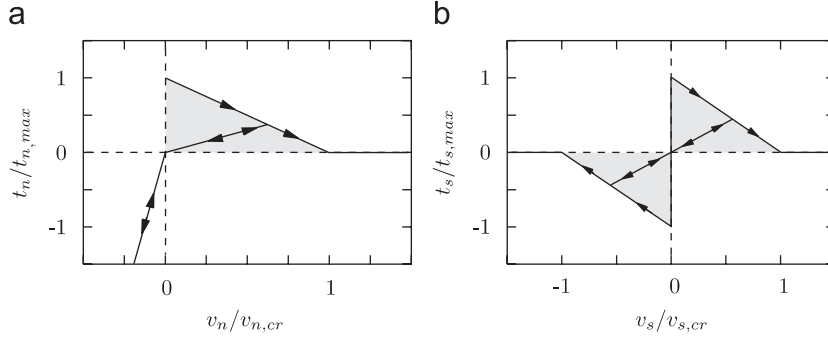


Fig. 6. The normalised tractions across the discontinuity as a function of the corresponding component of the displacement jump for a mode-I cleavage crack (a) and a shear crack (b) (Camacho and Ortiz, 1996).

The characteristic length of the cohesive law is determined by the critical normal opening displacement  $v_{n,cr}$  at which the crack has fully developed and the tractions have reduced to zero. This parameter is related to the fracture toughness  $\mathcal{G}_c$ , or the area under the softening curve and can be determined as follows:

$$v_{n,cr} = \frac{2\mathcal{G}_c}{t_{n,0}}. \quad (32)$$

When after some opening displacement  $v_{n,1}$ , the crack starts to close due to local unloading, the following relation is applied:

$$t_n = t_{n,0} \left(1 - \frac{v_{n,1}}{v_{n,cr}}\right) \frac{v_n}{v_{n,1}}, \quad t_s = t_{s,0} \left(1 - \frac{v_{n,1}}{v_{n,cr}}\right) \frac{v_n}{v_{n,1}} \operatorname{sgn}(v_s). \quad (33)$$

When during unloading the normal opening  $v_n$  becomes negative, self-contact is simulated by using a penalty stiffness  $D$ :

$$t_n = Dv_n \quad \text{if } v_n < 0. \quad (34)$$

Once the normal displacement jump exceeds the critical opening  $v_{n,cr}$ , the tractions in both normal and shear directions are set to zero.

When the initial normal traction  $t_{0,n}$  is negative, the discontinuity is assumed to open in a shear mode. The shear tractions decay in a linear fashion from the initial value  $t_{s,0}$  to zero according to, see Fig. 6(b):

$$t_s = t_{s,0} \left(1 - \frac{|v_s|}{v_{s,cr}}\right) \operatorname{sgn}(v_s). \quad (35)$$

As in the tensile case, a linear relation is assumed for the reloading curve:

$$t_s = t_{s,0} \left(1 - \frac{|v_s|}{v_{s,cr}}\right) \frac{v_s}{|v_{s,1}|}. \quad (36)$$

#### 4. Solution procedure

The equilibrium equations are discretised in the time domain using a variant of the Newmark- $\beta$  explicit time integration scheme with  $\beta = 0$  (Belytschko et al., 1976):

$$\dot{\mathbf{d}}^{t+(1/2)\Delta t} = \dot{\mathbf{d}}^t + \frac{1}{2}\Delta t \ddot{\mathbf{d}}^t, \quad (37a)$$

$$\mathbf{d}^{t+\Delta t} = \mathbf{d}^t + \Delta t \dot{\mathbf{d}}^{t+(1/2)\Delta t}, \quad (37b)$$

$$\ddot{\mathbf{d}}^{t+\Delta t} = \mathbf{M}^{-1}(\mathbf{f}^{\text{ext},t+\Delta t} - \mathbf{f}^{\text{int},t+\Delta t}), \quad (37c)$$

$$\dot{\mathbf{d}}^{t+\Delta t} = \dot{\mathbf{d}}^{t+(1/2)\Delta t} + \frac{1}{2}\Delta t \ddot{\mathbf{d}}^{t+\Delta t}. \quad (37d)$$

In these equations  $\Delta t$  is the discrete time step and  $\mathbf{d}$  represents the total array of degrees of freedom in the system:  $\mathbf{d} = [\mathbf{a}, \mathbf{b}_1, \dots, \mathbf{b}_m]^T$ .

For wave equations, the time step is limited by the speed of the stress wave in the material, or the dilation speed  $c_d$ . In general, the simulation becomes unstable when the stress wave crosses a single element with a specific element length  $l_e$  within a time interval  $\Delta t$  so that

$$\Delta t_{cr} = \frac{l_e}{c_d}. \quad (38)$$

The calculation time of an explicit time integration procedure is reduced significantly by using a diagonal mass representation  $\mathbf{M}^{\text{diag}}$  in Eq. (37c). In such a matrix, all terms are zero except for the ones on the diagonal. The inverse of a diagonal matrix can easily be determined by taking the inverse of each diagonal component. As a result, the system of equations (37c) is no longer coupled and each degree of freedom  $i$  can be solved separately:

$$d_i^{t+\Delta t} = \frac{f_i^{\text{ext},t+\Delta t} - f_i^{\text{int},t+\Delta t}}{M_i^{\text{diag}}}. \quad (39)$$

There are several ways to construct a diagonal mass matrix in the cohesive segment formulation. The approach that is used here is to *lump* the mass matrix by replacing the diagonal term of the mass matrix by the total sum of the mass terms on the corresponding row. The off-diagonal terms are set to zero. In the case of a system with  $n$  unknowns, the diagonal mass matrix  $\mathbf{M}^{\text{diag}}$  can be written as

$$M_i^{\text{diag}} = \sum_j^n M_{ij}. \quad (40)$$

It can be seen from Eq. (19) that the mass matrix contains terms that couple the regular and additional degrees of freedom. By lumping the matrix, this information will be lost. In order to determine the effects of lumping, the different approaches are studied in the following example, which is based on a numerical test by Xu and Needleman (1994).

Consider the plane strain block in Fig. 7. It has dimensions  $L = 5 \text{ mm}$  and  $W = 10 \text{ mm}$  and is made of PMMA with Young's modulus  $E = 3.24 \text{ GPa}$ , Poisson's ratio  $\nu = 0.35$  and density  $\rho = 1190 \text{ kg/m}^3$ . The corresponding dilatational, shear and Rayleigh wave speeds can be obtained from the following relations (Freund, 1998):

$$c_d = \sqrt{\frac{E(1-\nu)}{\rho(1+\nu)(1-2\nu)}}, \quad c_s = \sqrt{\frac{E}{2\rho(1+\nu)}}, \quad c_R = c_s \frac{0.862 + 1.14\nu}{1+\nu}. \quad (41)$$

According to these relations, the dilatational, shear and Rayleigh wave speeds for the given material are  $c_d = 2090 \text{ m/s}$ ,  $c_s = 1004 \text{ m/s}$  and  $c_R = 938 \text{ m/s}$ , respectively.

The block is not supported and is loaded by an impact velocity  $\dot{u}$ , acting in the positive  $y$  direction on the top boundary of the block (at  $y = +L$ ). The impact velocity is increased linearly to a constant value  $V$  within

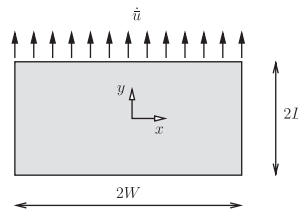


Fig. 7. Geometry and loading condition of the block.

a certain rise time  $t_r$ , according to

$$\dot{u} = \begin{cases} Vt/t_r & \text{for } t < t_r, \\ V & \text{for } t \geq t_r. \end{cases} \quad (42)$$

In this experiment, the rise time is taken to be  $t_r = 1.0 \times 10^{-7}$  s and the prescribed velocity  $V = 10$  m/s. The uniaxial stress wave created by these loading conditions will propagate through the block at approximately the dilatational wave speed,  $c_d = 2090$  m/s, carrying a tensile stress of 25.0 MPa.

Since the block and the loading conditions are symmetric about the  $y$ -axis, only the part in the positive  $x$ -axis is modelled using a regular mesh with  $39 \times 39$  four node elements. The specific length of each element is  $l_e = 0.256$  mm. The displacements in the  $x$ -direction of the nodes at  $x = 0.0$  mm are constrained in order to enforce symmetric boundary conditions. Regarding the specific length of an element and the magnitude of the dilatational wave speed, a sufficiently small time step of  $\Delta t = 1.0 \times 10^{-9}$  s has been used in the simulations, which have been performed using both a lumped and a consistent representation of the mass matrix. The nucleation and subsequent growth of cracks has not been taken into account in this experiment.

Fig. 8 shows the profile of the  $\sigma_{yy}$  stress along the  $y$ -axis at  $x = 0.0$  mm during the simulation. It can be seen that the average magnitude of the stress wave is in agreement with the analytical prediction of 25 MPa. The small stress oscillations of approximately 5.0 MPa can be attributed to the relatively coarse mesh that has been used in these simulations. The wave speed can be determined from the progression of the stress front with respect to time. Due to the numerical smoothing in the coarse mesh, the position of the stress wave cannot be determined very accurately. Nevertheless, a rough estimation reveals that the wave speed is in good agreement with the analytically obtained dilatational speed  $c_d = 2090$  m/s.

A remarkable difference between the simulations with the lumped mass matrix and the simulations with the consistent mass matrix is the appearance of the stress overshoot. The lumped mass matrix gives rise to an extra overshoot of approximately 5.0 MPa on top of the wave front of 25.0 MPa, whereas in the case of a consistent mass matrix, the stress wave is preceded by a dip of 5.0 MPa.

Subsequently, the block is divided into two parts by means of a horizontal crack at  $y = 0$  mm crossing the entire width of the specimen, Fig. 9. In the finite element analysis, this crack is represented as a traction free cohesive segment. In this particular case, the discontinuity is modelled using a standard Heaviside enhancement function, where  $\mathcal{H}^+ = 1$  and  $\mathcal{H}^- = 0$ , see Table 1. The boundary conditions and material parameters of the specimen, as well as the impact velocity are not changed.

In the simulations, the stress wave carrying a tensile stress of 25 MPa will propagate from the top side of the specimen to reach the crack after approximately  $t = 2 \mu\text{s}$ . Since the crack can be considered as a traction free boundary, the wave will reflect and move upwards. Obviously, the traction free crack prevents any kind of physical contact between the two parts of the specimen and the stresses in the lower part of the specimen will remain zero throughout the simulation.

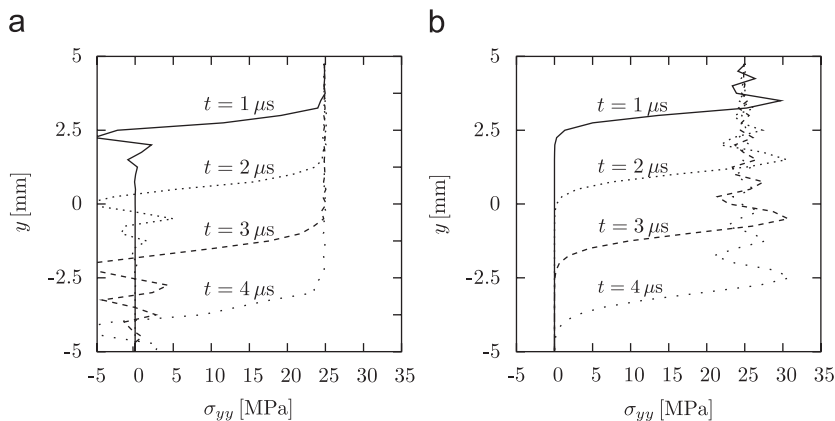


Fig. 8. Stress curves  $\sigma_{yy}$  versus vertical position  $y$  measured along the centre of the plane strain wave specimen ( $x = 0.0$  mm) at different times during the simulation: (a) consistent mass matrix; (b) lumped mass matrix.

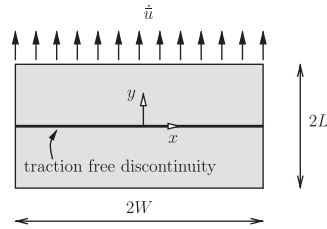


Fig. 9. Geometry and loading condition of the block with a traction free discontinuity: (a) Consistent mass matrix; (b) Lumped mass matrix.

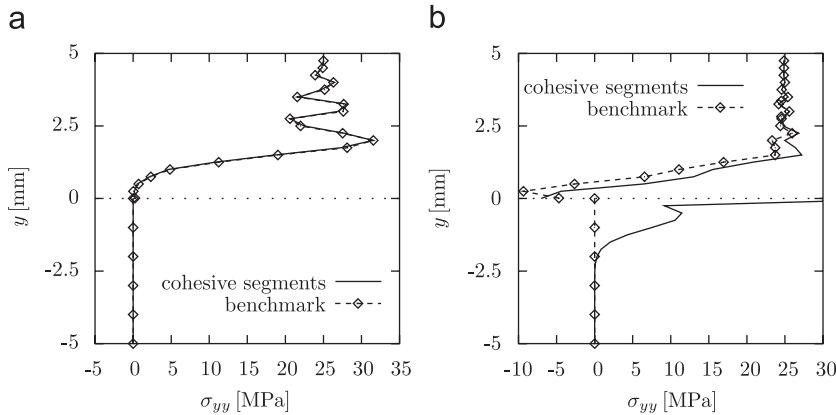


Fig. 10. Stress curves  $\sigma_{yy}$  versus vertical position  $y$  measured along the centre of the plane strain wave specimen ( $x = 0.0$  mm) at  $t = 3 \mu\text{s}$ . The initial crack (denoted by the dotted line) is modelled as a traction free cohesive segment which is constructed using a Heaviside jump function: (a) consistent mass matrix; (b) lumped mass matrix.

Fig. 10 shows the  $\sigma_{yy}$  stress curves along the  $y$ -axis in the centre of the specimen for both the case with a consistent mass matrix and that with a lumped mass matrix. In both graphs, the stress state at  $t = 3 \mu\text{s}$  is shown. At this instance, the stress wave has been reflected by the traction free crack. Both simulations are compared with a benchmark calculation in which the slit is modelled in the traditional way: by disconnecting adjacent elements. The benchmark calculations are performed using a consistent and a lumped mass matrix, respectively.

The simulation of the specimen with the crack using the consistent mass matrix shows perfect agreement with the benchmark simulation, see Fig. 10(a). The stress wave is properly reflected and, more importantly, the lower part of the specimen remains completely stress free. This is not the case in the simulation with a lumped mass matrix, Fig. 10(b). Here a considerable amount of the energy is transferred across the cohesive segment to result in a stress wave with an amplitude of 10 MPa in the lower part of the specimen. As a matter of fact, this spurious stress wave propagates with exactly the dilatation speed. There is also an extremely high stress peak of over 42 MPa in the integration points just below the discontinuity. Compared to this, the small mismatch of the stresses in the top part of the specimen, is a relatively minor discrepancy.

The simulations are now repeated with a different jump function. Instead of the Heaviside function a symmetric jump function is used, in which  $\mathcal{H}^+ = 1$  and  $\mathcal{H}^- = -1$ , Table 1. The corresponding traction profiles are shown in Fig. 11. Remarkably, the spurious stress wave reflections in the simulations with the lumped mass matrix representation have disappeared, Fig. 11(b). The stresses in the lower part of the specimen remain zero. Apparently, this can be contributed to the symmetric nature of the enhancement function. Nevertheless, the mismatch in the reflected stress wave in the top part of the specimen did not disappear, which reveals a small inconsistency in the current lumped matrix implementation. The stress waves in the simulation with the consistent mass matrix again show a perfect agreement to the benchmark simulations, see Fig. 11(a).

In sum, the simulations in which a consistent mass matrix is used give results that are identical to the benchmark simulations. When a lumped mass matrix is used, different jump functions to give rise to different

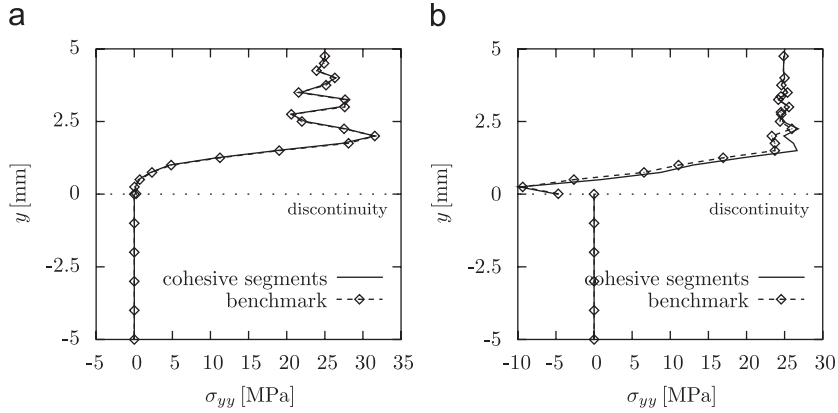


Fig. 11. Stress curves  $\sigma_{yy}$  versus vertical position  $y$  measured along the centre of the plane strain wave specimen ( $x = 0.0$  mm) at  $t = 3 \mu\text{s}$ . The initial crack (denoted by the dotted line) is modelled as a traction free cohesive segment which is constructed using a unit symmetric jump function: (a) consistent mass matrix; (b) lumped mass matrix.

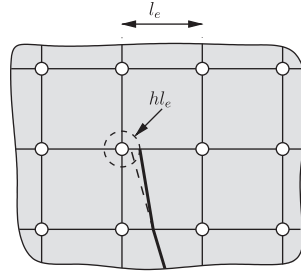


Fig. 12. Overview of the algorithm that prevents a discontinuity to cross an element boundary in the vicinity of a supporting node. The grey dashed line denotes the original position of the discontinuity. Since it crosses the node within a distance  $hl_e$  (denoted by the dashed circle), it is moved away from the node.

results. When the discontinuity is represented by a Heaviside function, spurious reflections of stress waves are observed. This is not the case with a unit-symmetric jump function. However, in both cases, the results are not identical to the benchmark calculations, which can be seen from the energy analysis. Since numerical accuracy is preferred over computational efficiency, all simulations in this paper are performed using a consistent mass matrix in combination with a Heaviside jump function.

The use of an explicit time integration scheme has another unpleasant consequence. When an element is crossed by a discontinuity, the two parts can be considered as individual elements, each with a smaller effective length  $l_e$  than the original element. An element can be crossed by a discontinuity in such a way that one of the two resulting parts of the element becomes so small that the critical time increment for a stable solution procedure will become almost infinitesimal. In order to avoid an infinitesimal critical increments, a discontinuity is not allowed to cross an element boundary within a certain distance  $hl_e$  to a node, where  $h$  is an offset factor between 0.0 and 0.5, see Fig. 12 (Remmers, 2006). Although the exact position of a new segment is slightly modified, it can be demonstrated that for reasonably small values of  $h$  the deflection is minimal. In the remaining simulations, an offset factor  $h = 0.1$  has been used. The corresponding deflection of the crack is then in the order of a few degrees. Because of the nearly linear relation between the critical time step and the distance between the discontinuity, the stability requirement can be expanded as follows:

$$\Delta t = \alpha \frac{hl_e}{c_d}, \quad (43)$$

where  $\alpha < 1$ . In the calculations here,  $\alpha = 0.1$  is used.

## 5. Examples

The performance of the cohesive segments method for dynamic loadings is assessed in three examples. First, the propagation of a single crack in a specimen loaded in tension is analysed. In this example, emphasis is put on the numerical consistency of the method. The second example deals with the propagation of a crack under shear loading. Finally, the ability to model crack branching is investigated in a bi-material specimen loaded in tension.

### 5.1. Crack propagation under tension

In the previous section, it was observed that the inclusion of a discontinuity in a finite element method can influence the robustness of the explicit time integration scheme. In the following example, the effects of *extending* a cohesive segment during a simulation is considered. Here, the attention is focused on the energy balance of the system.

Consider the square block with length sides  $L = 3 \text{ mm}$  as shown in Fig. 13. The block is made of PMMA with a Young's modulus  $E = 3.24 \text{ GPa}$ , Poisson's ratio  $\nu = 0.35$  and density  $\rho = 1190 \text{ kg/m}^3$  and contains an edge crack that penetrates  $a = 0.25 \text{ mm}$  into the material. The block is loaded in tension by two pulse loads that are applied to the top and bottom edges respectively. In the finite element calculation, these pulses are represented by prescribed velocities with magnitudes  $V = 6 \text{ m/s}$ . This magnitude is reached after a rise time  $t_r = 1.0 \times 10^{-7} \text{ s}$ , see Eq. (42). The fracture properties of the material are slightly modified to avoid a small cohesive length and therefore the necessity to use dense finite element meshes. In this simulation, the strength of the material is set to  $t_{\max} = 1.0 \times 10^8 \text{ N/m}^2$  and the fracture toughness  $\mathcal{G}_c = 700 \text{ N/m}$ . Because of symmetry, it is assumed that the crack will propagate in a straight line along the  $x$ -axis. The initiation criterion is modified such that the cohesive segment is extended when the  $\sigma_{yy}$  stress in the crack tip exceeds the strength  $t_{\max}$ . The stress state in the tip is determined by using the averaging function in which the averaging length  $l_a$  is taken to be two times the element length in the finite element mesh.

The block is analysed with three different finite element meshes that consist of quadrilateral elements only. In the first mesh, the specific length of an element is  $l_e = 37.5 \mu\text{m}$ , in the second mesh, which is depicted in Fig. 14, this length is  $l_e = 25.0 \mu\text{m}$  and in the third mesh  $l_e = 12.5 \mu\text{m}$ . In all simulations a timestep  $\Delta t = 1.0 \times 10^{-9} \text{ s}$  is used. The initial edge crack is modelled as a traction free cohesive segment. When the segment is extended, its opening is governed by the Camacho–Ortiz cohesive law, see Eq. (30).

Since in this case the trajectory of the crack is known beforehand, a benchmark calculation has also been performed in which the crack is modelled as a weak interface. In this benchmark calculation, a cohesive segment is inserted over the full width of the specimen at the onset of the analysis. The first  $0.25 \text{ mm}$  of this segment are traction free, the remaining part is equipped with a mixed-mode interface constitutive relation (Xu and Needleman, 1994), with the same cohesive properties as mentioned above. Apart from the fact that the cohesive surface in this case has an initial non-zero compliance, the overall behaviour is expected to be the same as for an initially rigid cohesive surface.

The accuracy of the method can be checked by examining the energy balance of the system, i.e. the amount of external work that is used to deform the specimen must be equal to the total internal energy, which is

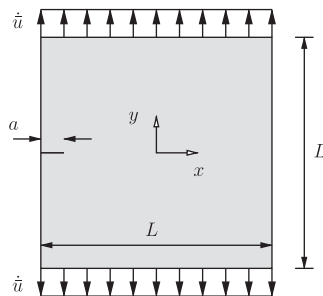


Fig. 13. Geometry and loading conditions of a square block with an initial side crack.

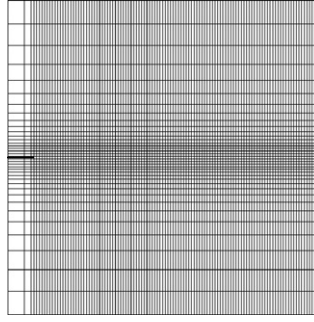


Fig. 14. Finite element mesh of the square block with an initial side crack, indicated by the bold line. The specific length of the elements in the zone through which the crack will propagate is  $l_e = 25.0 \mu\text{m}$ .

composed of the strain energy and the kinetic energy. In this specific case, a distinction is made between the contribution of the bulk material and the cohesive segments to the strain energy:

$$\mathcal{E}_{\text{int}} = \mathcal{E}_{\text{bulk}} + \mathcal{E}_{\text{coh}}, \quad (44)$$

where  $\mathcal{E}_{\text{bulk}}$  is the strain energy of the bulk material, which is defined as

$$\mathcal{E}_{\text{bulk}}^{t+\Delta t} = \mathcal{E}_{\text{bulk}}^t + \frac{1}{2}\Delta t(\dot{\mathbf{d}}^{t+(1/2)\Delta t})^T(\mathbf{f}_{\text{bulk}}^{\text{int},t} + \mathbf{f}_{\text{bulk}}^{\text{int},t+\Delta t}), \quad (45)$$

where  $\mathbf{f}_{\text{bulk}}^{\text{int}}$  is the contribution of the *bulk material* to the internal forces, see Eqs. (23) and (24). For the cohesive segments, a similar relation can be formulated:

$$\mathcal{E}_{\text{coh}}^{t+\Delta t} = \mathcal{E}_{\text{coh}}^t + \frac{1}{2}\Delta t(\dot{\mathbf{d}}^{t+(1/2)\Delta t})^T(\mathbf{f}_{\text{coh}}^{\text{int},t} + \mathbf{f}_{\text{coh}}^{\text{int},t+\Delta t}), \quad (46)$$

where  $\mathbf{f}_{\text{coh}}^{\text{int}}$  is the contribution of the *cohesive segments* to the internal forces, see (23). The external work  $\mathcal{W}$  due to a pulse load can be written as

$$\mathcal{W}^{t+\Delta t} = \mathcal{W}^t + \frac{1}{2}\Delta t(\dot{\mathbf{d}}_p^{t+(1/2)\Delta t})^T(\mathbf{f}^{\text{int},t} + \mathbf{f}^{\text{int},t+\Delta t}), \quad (47)$$

where  $\dot{\mathbf{d}}_p^{t+(1/2)\Delta t}$  denotes the prescribed velocity vector in which the unconstrained degrees of freedom are replaced by zeros. The kinetic energy is given by

$$\mathcal{E}_{\text{kin}}^t = \frac{1}{2}(\dot{\mathbf{d}}^t)^T \mathbf{M} \dot{\mathbf{d}}^t. \quad (48)$$

Energy conservation requires that the sum of internal and kinetic energy is equal to the total external work, or

$$|\mathcal{E}_{\text{kin}} + \mathcal{E}_{\text{int}} - \mathcal{W}| < \varepsilon \max(|\mathcal{W}|, |\mathcal{E}_{\text{int}}|, \mathcal{E}_{\text{kin}}), \quad (49)$$

where  $\varepsilon$  is a small tolerance. When this tolerance is on the order of  $10^{-2}$  or smaller, it can be concluded that energy is conserved (Belytschko et al., 2000).

Fig. 15(a) shows the variations of the total work  $\mathcal{W}$ , the sum of internal energies  $\mathcal{E}_{\text{tot}}$  and the variations of the individual terms  $\mathcal{E}_{\text{bulk}}$ ,  $\mathcal{E}_{\text{coh}}$  and  $\mathcal{E}_{\text{kin}}$  for the benchmark simulation with a predefined cohesive segment in combination with Xu–Needleman’s cohesive relation, i.e. the simulation in which no degrees of freedom are added during the simulation. In this figure, the energy variations of the simulation with the dense mesh are shown, but the results with the coarser meshes are nearly identical. Figs. 15(b) to (d) show the variations of the energies in the cohesive-segments simulations with the coarse, medium and dense meshes, respectively. It appears that in all four cases, the total internal energy is in good agreement with the external work of the simulations. This can also be seen in Fig. 16 in which the error tolerances as defined in Eq. (49) are plotted.

In all simulations, the error tolerance is initially very large. This can be contributed to the fact that the energy components in the first microseconds of the simulation are relatively small, causing a near zero division. In the remainder of the simulation,  $\varepsilon$  never exceeds 0.01. Accordingly, irrespective of the coarseness of the finite element mesh, the creation of new degrees of freedom does not destroy the energy balance. This is a result of the fact that in the cohesive constitutive relation, the value of the strength  $t_{n,0}$  is taken to be equal to

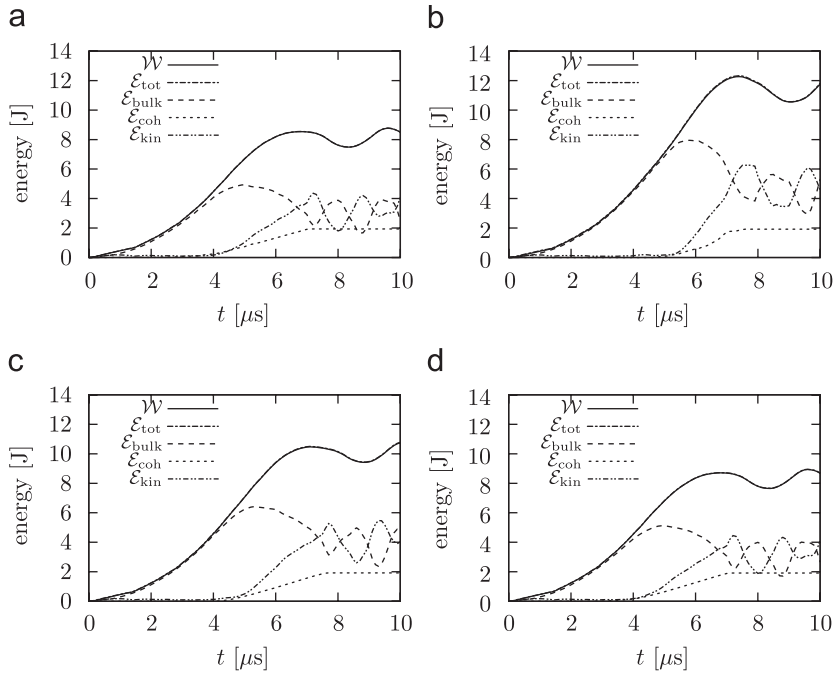


Fig. 15. Energy variations as a function of time. (a) shows the benchmark simulation with an initial cohesive segment with Xu–Needleman’s cohesive relation. The other figures show the calculations with a propagating cohesive segment in meshes with different specific element lengths (b) 37.5, (c) 25.0 and (d) 12.5  $\mu\text{m}$ .

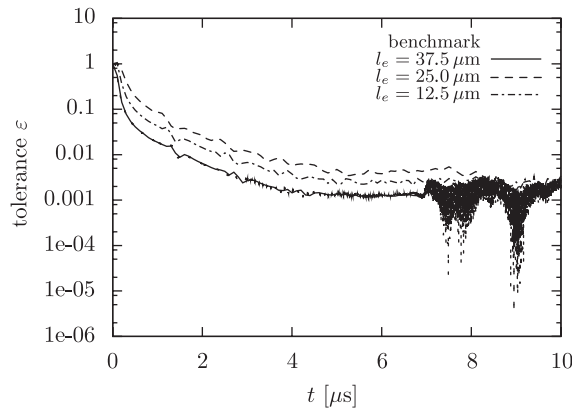


Fig. 16. Energy tolerances as a function of time for the four simulations of a propagating straight crack through a square block.

the stress state that caused the cohesive segment to propagate. No effects of overshoot are seen and stress continuity appears to occur (Papoulia et al., 2003).

Nevertheless, a significant difference is observed in the simulations with the coarser meshes, Fig. 15(b) and (c). Here, the total work is significantly larger than the total work in the benchmark simulation (a) and the simulation with the dense mesh (d). This is a consequence of the fact that the averaging length  $l_a$  in these simulations is of the same order of magnitude, or even larger, than the cohesive length. As a result, the new segment is extended too late, allowing the bulk material to store too much internal energy prior to crack propagation. This can also be concluded from Fig. 17 where the position of the crack tip is plotted as a function of time. Here, the position of the crack tip is defined as the first point along the cohesive segment



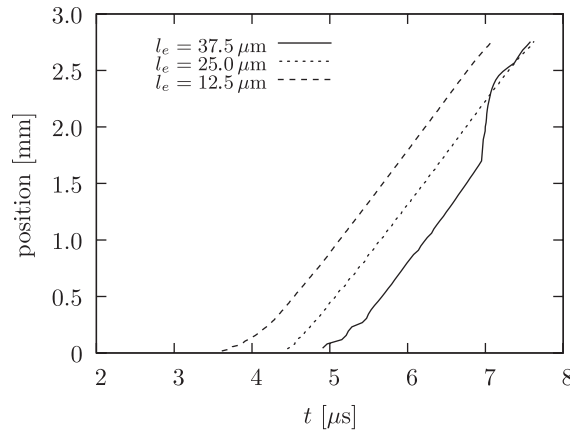


Fig. 17. Position of the crack tip as a function of time for the four simulations of a propagating straight crack through a square block.

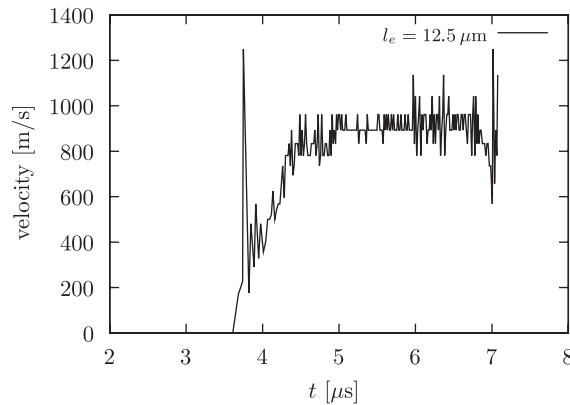


Fig. 18. Velocity of the crack tip as a function of time for the simulation with the  $l_e = 12.5 \mu\text{m}$ .

where the tractions have reduced to 5% the value of the strength of the material. In the simulations with the coarser meshes, the onset of crack propagation is somewhat delayed.

Fig. 18 shows the velocity of the crack tip as a function of time. It can be seen that the crack tip quickly accelerates to the Rayleigh wave speed of the material,  $c_R = 938 \text{ m/s}$ . In this figure, only the graph of the simulation with the most refined finite element mesh is shown: the graphs of the simulations with the coarser meshes show extreme velocity peaks. This is because the elements are too large compared to the length of the cohesive zone. In these situations, the cohesive segment is extended over a few elements in a small period of time (three extensions in three consecutive time steps is not uncommon) and subsequently remains stationary for a longer period.

The coarseness of the mesh does not have an effect on the internal energy dissipated by the cohesive segment. In all simulations with a propagating segment, the final value of the cohesive internal energy  $\mathcal{E}_{\text{coh}}$ , when the crack has completely crossed the specimen is equal to  $\mathcal{E}_{\text{coh}} = 1.92 \text{ J}$ , which is exactly identical to the length of the crack,  $2.75 \text{ mm}$  times the fracture toughness of the material  $\mathcal{G}_c = 700 \text{ N/m}$ . In the benchmark simulation, with an initial cohesive segment, this value is slightly larger,  $\mathcal{E}_{\text{coh}} = 1.93 \text{ J}$ , which is probably due to the fact that prior to cracking, the cohesive zone, with its initial non-zero compliance, already contributes to the internal energy.

The stress distribution and the deformed mesh are shown in Fig. 19. In this picture, the results of the simulation with a propagating cohesive segment in a finite element mesh with  $l_e = 12.5 \mu\text{m}$  are depicted.

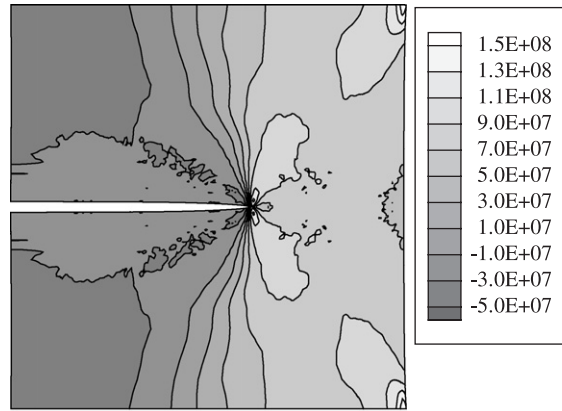


Fig. 19. The deformed specimen and the  $\sigma_{yy}$  stress distribution at  $t = 5.0 \mu s$  for the simulation with a propagating cohesive segment  $l_e = 12.5 \mu m$ .

## 5.2. Dynamic shear failure

An experimental set-up for subjecting edge cracks in plate specimens to high rate shear loading has been proposed by Kalthoff and Winkler (1988) and related configurations have been used subsequently in a variety of investigations, e.g. (Mason et al., 1994) and (Ravi-Chandar, 1995). At sufficiently high rates of loading, fracture in this configuration takes place by cleavage cracking at an angle of approximately  $60-70^\circ$  with respect to the initial crack. This type of failure has been modelled by Needleman and Tvergaard (1995) and Li et al. (2002). At higher impact velocities, the crack propagates as an adiabatic shear band at an angle of approximately  $-5^\circ$  with respect to the original crack (Kalthoff and Bürgel, 2004). Here, we explore the use of the cohesive segments method to analyse the configuration shown in Fig. 20 although since the material is modelled as linear elastic adiabatic shear banding cannot be modelled.

The specimen in the figure has dimensions  $L = 0.003 m$  and  $W = 0.0015 m$  and has an initial crack with length  $a = 0.0015 m$ . It consists of an isotropic linear elastic material with Young's modulus  $3.24 \times 10^9 N/m^2$ , Poisson's ratio  $0.35$  and density  $\rho = 1190.0 kg/m^3$ . The corresponding dilatational, shear and Rayleigh wave speeds are  $c_d = 2090 m/s$ ,  $c_s = 1004 m/s$  and  $c_R = 938 m/s$ , respectively. The ultimate normal traction of the material is set to  $100.0 \times 10^6 N/m^2$  and the fracture toughness is  $700 N/m$ . The lower part of the specimen is subjected to an impulse load in the positive  $x$ -direction which is modelled as a prescribed velocity with magnitude  $V$  with a rise time  $t_r = 0.1 \mu s$ , see Eq. (42).

The specimen is discretised using quadrilateral elements. In the region around the crack tip, the mesh is locally refined such that the specific length of the elements equals  $l_e = 15.0 \mu m$ , see Fig. 21. According to Eq. (43), the time increment is set to  $\Delta t = 1.0 \times 10^{-10} s$ . At the start of the simulation, the finite element mesh contains 11587 degrees of freedom. The initial crack is modelled as a traction free discontinuity and therefore, in contrast with the simulations done by Needleman and Tvergaard (1995), the crack tip is sharp. The possibility of crack nucleation away from the main crack tip is not taken into account.

The specimen is loaded with three different impact velocities profiles  $\tilde{u}$ , see Eq. (42), with maximum values  $V = 25, 40$  and  $55 m/s$ . In all cases, the rise time is taken  $t_r = 1.0 \times 10^{-7}$ . The trajectories of the cracks are shown in Fig. 22. The corresponding positions of the crack tips as a function of time are shown in Fig. 23. In this graph, the position of the crack tip is the sample point on the cohesive segment that has just become traction free. Clearly, this point is not the same as the actual tip of the cohesive segment.

In the case of  $V = 25 m/s$ , the cohesive segment is extended for the first time at  $t = 3.01 \mu s$  at an angle of roughly  $65^\circ$ , which is in agreement with experimental observations (Kalthoff and Winkler, 1988). At  $t \approx 3.7 \mu s$  the propagation of the crack slows down and the orientation of the trajectory changes to  $50^\circ$ . This small deviation is caused by a reflection of the initial compressive stress wave which travels through the specimen in the horizontal direction at the dilatational speed  $c_d$ . At approximately  $3.7 \mu s$  after impact, this stress waves passes the region just to the right of the original crack tip for the third time. The additional compressive stress

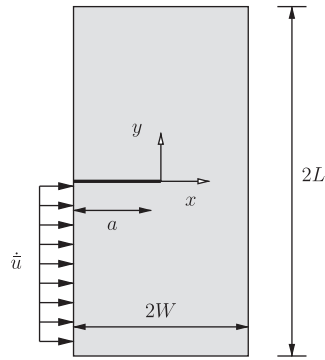


Fig. 20. Geometry and loading conditions of the specimen for the dynamic shear failure test.

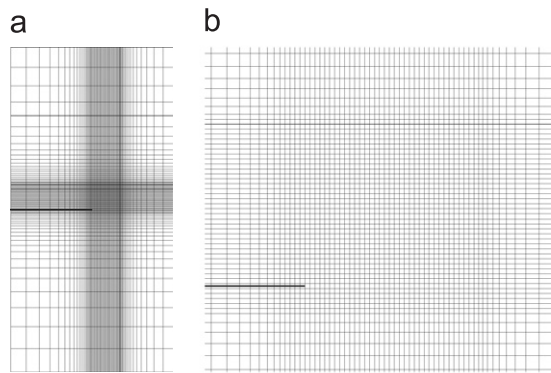


Fig. 21. Finite element mesh of the dynamic shear failure experiment. The initial crack is modelled as a cohesive segment, which is denoted by the bold line. The specific length of the elements ahead of the crack tip is  $l_e = 15.0 \mu\text{m}$ : (a) full mesh; (b) detail of crack tip region.

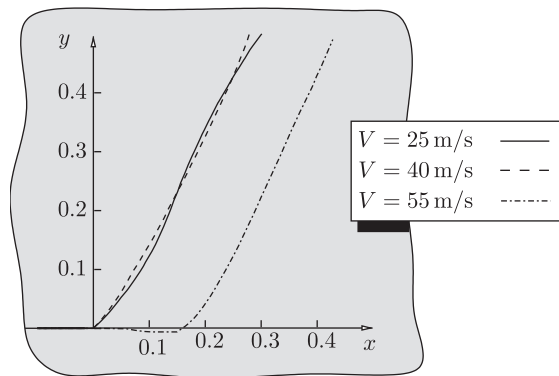


Fig. 22. The trajectory of the cracks in the dynamic shear failure simulation for different impact velocities. The original crack tip was located at the origin of the coordinate system. All dimensions in millimetres.

changes the stress state at the current crack tip and therefore the angle of the principal stress. Once this wave has passed, the crack trajectory continues at an angle of approximately  $65^\circ$ . Fig. 24 shows the position of the crack and the corresponding stress contours at various instances during the simulation.

When  $V = 40 \text{ m/s}$ , the trajectory of the crack is almost a straight line. Apparently, the direction of the crack is less influenced by reflecting stress waves. When the specimen is loaded by an impact load with  $V = 55 \text{ m/s}$ ,

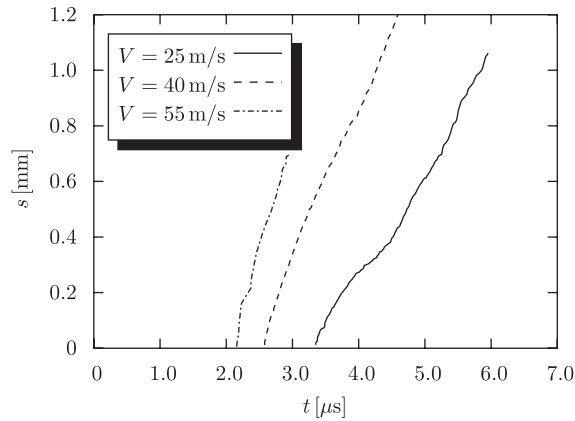


Fig. 23. Crack length  $s$  versus time for different impact velocities. Distance  $s$  is measured with respect to the original crack tip.

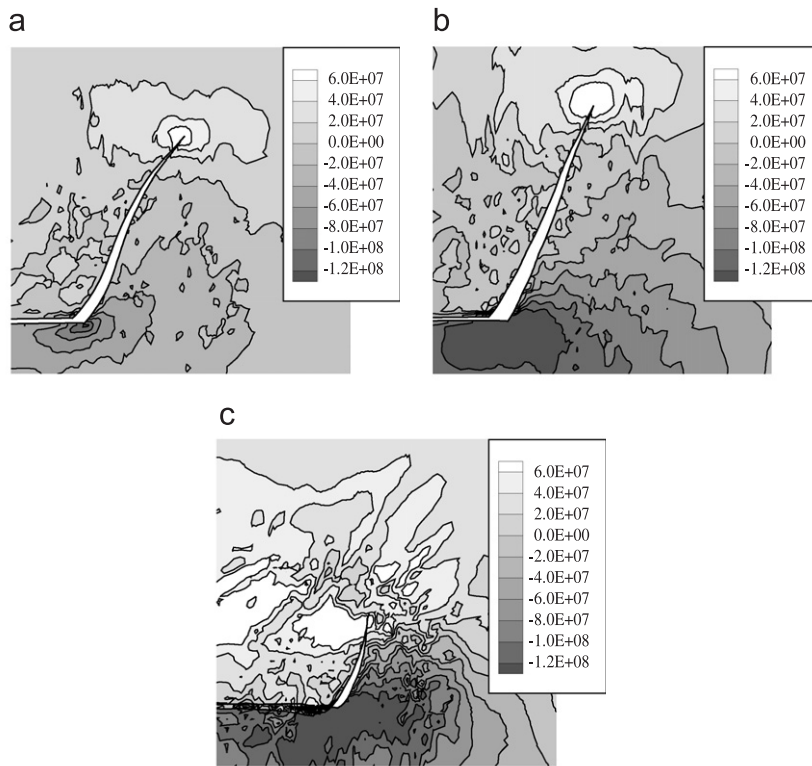


Fig. 24. Deformed specimen and  $\sigma_{xx}$  stresses of the dynamic shear failure experiment under different impact velocities  $V$ . All stresses in  $[\text{N/m}^2]$ : (a)  $V = 25 \text{ m/s}$ ,  $t = 4.8 \mu\text{s}$ ; (b)  $V = 40 \text{ m/s}$ ,  $t = 3.6 \mu\text{s}$ ; (c)  $V = 55 \text{ m/s}$ ,  $t = 2.56 \mu\text{s}$ .

the crack will not propagate at an angle of  $70^\circ$ , but initially propagates along the initial crack line before deviating. In the experiments, the more nearly straight ahead mode is associated with an adiabatic shear band, but in the analysis here, the bulk material has been modelled as linear elastic, so that adiabatic shear banding is not modelled.

Fig. 24 shows the deformed specimen and the  $\sigma_{xx}$  stress distribution at the end of the simulation for the three different loading cases. Note that in the simulation with  $V = 55 \text{ m/s}$ , the crack initially has a negative

normal displacement jump. This could have been avoided by extending the initial traction free discontinuity with a contact law. However, since the shear jump displacements in this region are of the order of 10 times the element length  $l_e$ , the use of such a contact algorithm would no longer be correct from a physical point of view.

### 5.3. Crack growth along an interface

The specimen in Fig. 25 consists of two parts with different elastic material properties that are bonded along  $y = 0$  with a centre crack along the bond line. The dimensions of the specimen are  $2W = 12$  mm and  $2L = 6$  mm. The centre crack measures  $2a = 2$  mm. The top and bottom edges of the specimen are subjected to impact loads that are modelled as prescribed velocities that increase linearly to a value  $V = 20$  m/s with a rise time  $t_r = 10^{-7}$  s.

The top part of the specimen consists of a material with Young's modulus  $E = 3.24 \times 10^9$  N/m<sup>2</sup>. The Poisson's ratio is  $\nu = 0.3$  and the density is  $\rho = 1190$  kg/m<sup>3</sup>. The material properties of the lower part are:

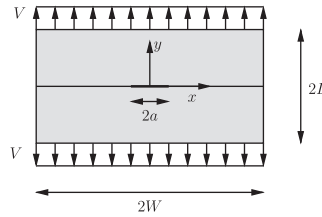


Fig. 25. Geometry and loading conditions of the interface crack growth specimen.

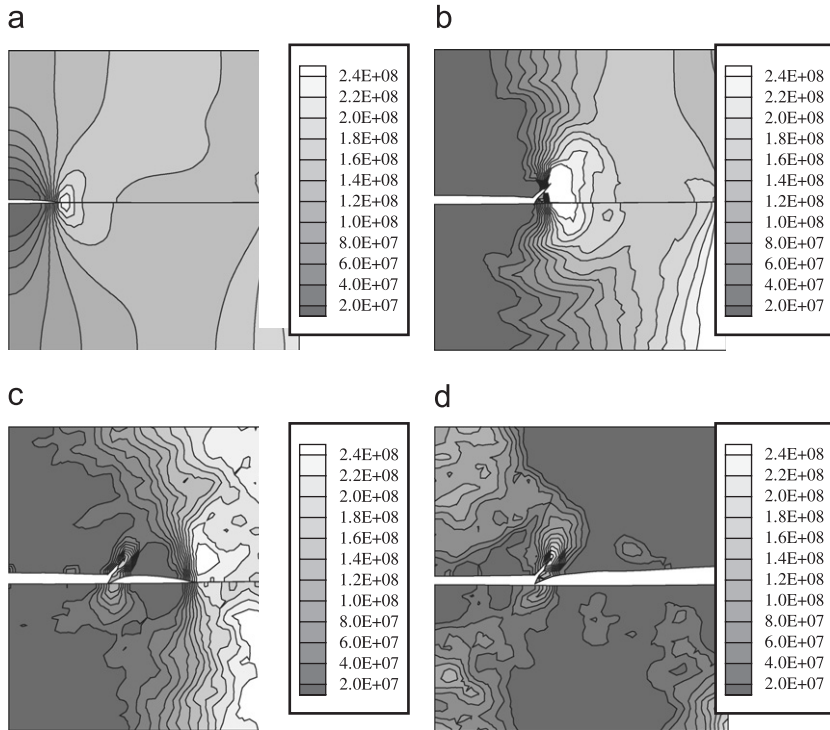


Fig. 26. Evolution of fracture in the bi-material specimen. The colour gradient represents the  $\sigma_{yy}$  stresses [N/m<sup>2</sup>]. (a) Onset of debonding at the interface. (b) Creation of a new cohesive segment in the bulk material. This new segment is created at an angle of  $68^\circ$  with respect to the interface. (c) Continuation of debonding of the interface as a daughter crack ahead of the current crack tip. (d) Total failure of the specimen: (a)  $t = 2.0$   $\mu$ s; (b)  $t = 2.3$   $\mu$ s; (c)  $t = 2.8$   $\mu$ s; (d)  $t = 3.3$   $\mu$ s.

$E = 12.2 \times 10^9 \text{ N/m}^2$ ,  $\nu = 0.3$  and  $\rho = 1190 \text{ kg/m}^3$ , respectively. The interface is represented by a cohesive segment with Xu–Needleman’s constitutive relation with  $t_{\max} = 3.24 \times 10^8 \text{ N/m}^2$  and  $\mathcal{G}_c = 700 \text{ N/m}$ . At the initially debonded part, a traction free constitutive relation is used. In the simulation, cracks are allowed to nucleate in the top part of the specimen. Here, the fracture properties are  $t_{\max} = 410 \times 10^6 \text{ N/m}^2$  and  $\mathcal{G}_c = 700 \text{ N/m}$ .

Because of symmetry along the  $y$ -axis, only one half of the specimen is modelled. The relatively coarse mesh consists of  $39 \times 39$  four node elements, the time step chosen to be  $\Delta t = 1.0 \times 10^{-9} \text{ s}$ .

Upon loading, after approximately  $t = 2.0 \mu\text{s}$ , the interface starts to debond, see Fig. 26(a). The stress state around the crack tip soon builds up to a level such that a new cohesive segment nucleates in the top half of the specimen, Fig. 26(b). This segment crosses the interface at an angle of approximately  $65^\circ$  with the interface. This new segment has a finite length of two elements. During the creation and opening of this branch, the debonding of the interface arrests. However, the new cohesive segment is not extended and the branch seems to arrest. Instead, after some time, the interface starts to debond away from the branch position as a so-called daughter crack, similar to the fracture pattern observed in (Coker et al., 2003), Fig. 26(c). After  $3.3 \mu\text{s}$  the interface has completely debonded and the specimen has lost its load carrying capability.

A mesh refinement study suggests that the reason for the branch arresting may not be of a physical origin, but may be related to the numerical method. Both the nucleation of a crack, as well as its extension, are controlled by the same criterion. However, in order to arrive at a reliable stress state in the tip of a cohesive segment, the stresses are determined by averaging them. As a result, the tip stress is slightly lower than the actual local stress and a higher stress state is needed to extend a segment. The nucleation of a new cohesive segment, however, is determined by the exact stress state in an integration point in the bulk material.

In dynamic simulations, the instant of crack propagation appears to be an important factor. In the case of two competing cracks, as displayed in this example, the slight unbalance in propagation criterion can result in spurious crack arrest.

## 6. Conclusions

The cohesive segments method has been used to simulate fast crack propagation in brittle solids. Special attention is paid to the implementation of the method in a Newmark- $\beta$  explicit time integration scheme. An important conclusion is that, in contrast to more traditional finite element approaches, there can be a significant loss of accuracy using a lumped mass matrix. When a Heaviside jump function is used, spurious transfer of tractions has been observed. This loss of accuracy is considerably reduced when the Heaviside function is replaced by a unit-symmetric jump function. However, from an energetic point of view, the numerical results still show small errors.

Additional studies show that adding degrees of freedom during a simulation, does not affect the energy conservation. Even in the case of relatively coarse meshes, the internal and kinetic energies of the system sum up to the total external work.

The performance of the cohesive segments method is illustrated in the dynamic shear test. For modest impact velocities, the crack propagates at an angle of approximately  $70^\circ$  with the initial crack, which is in agreement with various experimental observations and analytical studies. Even small deviations of this trajectory due to reflecting stress waves are captured. Straight ahead crack growth can also occur, but since the material is modelled as linear elastic, the adiabatic shear band observed experimentally under high impact velocities, is not modelled. The final example demonstrates the ability of the method to capture crack nucleation in the vicinity of an interface. We expect that this algorithm also accommodates the simulation of crack branching including  $Y$ -crack bifurcations as discussed in (Xu and Needleman, 1994), although this remains to be demonstrated.

The criterion that is used to calculate the stress state at the tip of a segment is still a point of concern. Due to stress averaging, it is not possible to determine the exact impact velocity that marks the crack growth mode transition in the dynamic shear test. It also hampers a quantitative analysis in the case of multiple, interacting cracks, as shown in the analysis of crack growth along and off of a bi-material interface. However, it is not clear if the branched crack arrested for physical reasons, or because of shortcomings of the crack propagation algorithm.

## Acknowledgements

We are pleased to acknowledge insightful comments and helpful suggestions from Professor Emily Carter of Princeton University during an oral presentation of this work.

## References

- Babuška, I., Melenk, J.M., 1997. The partition of unity method. *Int. J. Numer. Methods Eng.* 40 (4), 727–758.
- Belytschko, T., Black, T., 1999. Elastic crack growth in finite elements with minimal remeshing. *Int. J. Numer. Methods Eng.* 45 (5), 601–620.
- Belytschko, T., Chiapetta, R.L., Bartel, H.D., 1976. Efficient large scale non-linear transient analysis by finite elements. *Int. J. Numer. Methods Eng.* 10 (3), 579–596.
- Belytschko, T., Liu, W.K., Moran, B., 2000. *Nonlinear Finite Elements for Continua and Structures*. Wiley, England.
- Camacho, G.T., Ortiz, M., 1996. Computational modelling of impact damage in brittle materials. *Int. J. Solids Struct.* 33, 2899–2938.
- Coker, D., Rosakis, A.J., Needleman, A., 2003. Dynamic crack growth along a polymer composite-homalite interface. *J. Mech. Phys. Solids* 51 (3), 425–460.
- Daux, C., Moës, N., Dolbow, J., Sukumar, N., Belytschko, T., 2000. Arbitrary branched and intersecting cracks with the extended finite element method. *Int. J. Numer. Methods Eng.* 48 (12), 1741–1760.
- Falk, M.L., Needleman, A., Rice, J.R., 2001. A critical evaluation of cohesive zone models of dynamic fracture. *J. Phys. IV* 11 (Pr5), 43–50.
- Freund, L.B., 1998. *Dynamic Fracture Mechanics*. Cambridge University Press, Cambridge.
- Gao, H.J., 1993. Surface roughening and branching instabilities in dynamic fracture. *J. Mech. Phys. Solids* 41, 457–486.
- Gao, H.J., 1996. A theory of local limiting speed in dynamic fracture. *J. Mech. Phys. Solids* 44, 1453–1474.
- Kalthoff, J.A., Bürgel, A., 2004. Influence of loading rate on shear fracture toughness for failure mode transition. *Int. J. Impact Eng.* 30, 957–971.
- Kalthoff, J.K., Winkler, S., 1988. Failure mode transition at high rates of loading. In: Chiem, C.Y., Kunze, H.D., Meyer, L.W. (Eds.), *Proceedings of the International Conference on Impact Loading and Dynamic Behaviour of Materials*. Deutsche Gesellschaft für Metallkunde, pp. 43–56.
- Li, S.F., Liu, W.K., Rosakis, A.J., Belytschko, T., Hao, W., 2002. Mesh free Galerkin simulation of dynamic shear band propagation and failure mode transition. *Int. J. Solids Struct.* 39, 1213–1240.
- Mason, J.J., Rosakis, A.J., Ravichandran, G., 1994. Full field measurements of the dynamic deformation field around a growing adiabatic shear band at the tip of a dynamically loaded crack or notch. *J. Mech. Phys. Solids* 42, 1679–1697.
- Needleman, A., 1987. A continuum model for void nucleation by inclusion debonding. *J. Appl. Mech.* 54, 525–531.
- Needleman, A., Tvergaard, V., 1995. Analysis of a brittle-ductile transition under dynamic shear loading. *Int. J. Solids Struct.* 32, 2571–2590.
- Papoulia, K.D., Sam, S.H., Vavasis, S.A., 2003. Time-continuous cohesive interface finite elements in explicit dynamics. *Int. J. Numer. Meth. Eng.* 58 (5), 679–701.
- Papoulia, K.D., Vavasis, S.A., Ganguly, P., 2006. Spatial convergence of crack nucleation using a cohesive finite element model on a pinwheel-based mesh. *Int. J. Numer. Meth. Eng.* 67, 1–16.
- Ravi-Chandar, K., Knauss, W.G., 1984. An experimental investigation into dynamic fracture: I: crack initiation and arrest. *Int. J. Frac.* 25 (4), 247–262.
- Ravi-Chandar, K., 1995. On the failure mode transitions in polycarbonate under dynamic mixed-mode loading. *Int. J. Solids Struct.* 32, 925–938.
- Remmers, J.J.C., 2006. *Discontinuities in Materials and Structures, A unifying computational approach*. Ph.D. Dissertation, Delft University of Technology, Delft, The Netherlands.
- Remmers, J.J.C., deBorst, R., Needleman, A., 2003. A cohesive segments method for the simulation of crack growth. *Comput. Mech.* 31, 69–77.
- Sharon, E., Fineberg, J., 1999. The dynamics of fast fracture. *Adv. Eng. Mater.* 1, 119–122.
- Sharon, E., Gross, S.P., Fineberg, J., 1995. Local crack branching as a mechanism for instability in dynamic fracture. *Phys. Rev. Lett.* 74, 5096–5099.
- Wells, G.N., Sluys, L.J., 2001. A new method for modelling cohesive cracks using finite elements. *Int. J. Numer. Methods Eng.* 50 (12), 2667–2682.
- Xu, X.P., Needleman, A., 1994. Numerical simulations of fast crack growth in brittle solids. *J. Mech. Phys. Solids* 42, 1397–1434.